Excitation Modalities for Enhanced Micro and Nanoparticle Imaging in a Smartphone Coupled 3D Printed Fluorescent Microscope

Journal:	*Lab on a Chip*
Manuscript ID	LC-ART-06-2022-000589.R1
Article Type:	Paper
Date Submitted by the Author:	22-Aug-2022
Complete List of Authors:	Sami, Muhammad Ahsan; Rutgers The State University of New Jersey, Electrical & Computer Engineering Tayyab, Muhammad; Rutgers The State University of New Jersey, Electrical and Computer Engineering Hassan, Umer; Rutgers The State University of New Jersey, Electrical and Computer Engineering

SCHOLARONE™
Manuscripts

Excitation Modalities for Enhanced Micro and Nanoparticle Imaging in a Smartphone Coupled 3D Printed Fluorescent Microscope

Authors: Muhammad A. Sami[1], Muhammad Tayyab[1], and Umer Hassan*[1, 2]

[1] Department of Electrical and Computer Engineering, School of Engineering, Rutgers, The State University of New Jersey, United States of America.

[2] Global Health Institute, Rutgers, The State University of New Jersey, New Brunswick, United States of America.

 *Corresponding Author: umer.hassan@rutgers.edu (UH); Tel (848) 445-2164

Abstract

Smartphone fluorescent microscopes (SFM) offer many functional characteristics similar to their benchtop counterparts at a fraction of the cost and have been shown to work for biomarker detection in many biomedical applications. However, imaging and quantification of bioparticles in sub-micron and nanometer range remains challenging as it requires aggressive robustness and high-performance metrics of the building blocks of SFM. Here, we explored multiple excitation modalities and their performance on the imaging capability of an SFM. Employing spatial positional variations of the excitation source with respect to image sample plane (i.e., parallel, perpendicular, oblique) we developed three distinct SFM variants. These SFM variants were tested using green-fluorescent beads of four different sizes (8.3, 2, 1, 0.8 μm). Optimal excitation voltage range was determined by imaging these beads at multiple excitation voltages to optimize for no data loss and acceptable noise levels for each SFM variant. The SFM with parallel excitation was able to only image 8.3 μm beads while the SFM variants with perpendicular and oblique excitation were able to image all four bead sizes. Relative performance of the SFM variants was quantified by calculating signal difference to noise ratio (SDNR) and contrast to noise ratio (CNR) from the captured images. SFM with oblique excitation generated the highest SDNR/CNR values, whereas, for power consumption, SFM with perpendicular excitation generated the best results. This study sheds light on significant findings related to performance of SFM systems and their potential utility in biomedical applications involving sub-micron imaging. Similarly, findings of this study are translatable to benchtop microscopy instruments as well to enhance their imaging performance metrics.

Key Words: Smartphone fluorescence microscope (SFM), microparticles, nanoparticles, submicron imaging, signal difference to noise ratio (SDNR), contrast to noise ratio (CNR).

1. Introduction

Fluorescent microscopes are one of the most essential instruments present in any modern life sciences laboratory. These precision instruments find utility in a multitude of scientific disciplines such as biology, chemistry, and material science [1][2][3]. By functionalizing the surface of test molecules with different fluorescent probes, these instruments can be used for multiplexed analyte detection and quantification, a technique which is of particular importance in many biological applications e.g., cell viability and leukocyte imaging assays [4][5]. In addition to that, fluorescent microscopes are also routinely used in the detection and assessment of tumors and cancers [6]. Though fiercely efficient and precise, high cost, requirement of trained professionals for usage, and low mobility limit the use of these benchtop fluorescent microscopes at point of care (POC) and low resource settings.

Smartphone based fluorescent microscopes (SFM) have enhanced their mobility and offer many features offered by their benchtop counterparts at a fraction of cost. These devices, thus, have a great potential to be used at POC and low resource settings for diagnostics, environmental monitoring, or other therapeutic applications [7][8]. Over the years, the camera modules of modern-day smartphone devices keep getting improved and consequently, the performance of these SFMs also keeps on improving. Multiple studies depicting the usage of these SFM for diagnostic and therapeutic applications have been published in the past [9].

Recently, Kim et.al., presented the design and working of a smartphone microscopy system in conjunction with a paper-based platform for imaging and quantification of SARS-CoV-2 virus [10]. Similarly, in [11], the working and design of another fluorescent microscopy system capable of doing ELISA is discussed. This system employed a fluorescent enhancement strategy for the detection of *Opisthorchis viverrini* (Ov) antigen in urine samples. Furthermore, researchers in [12] discuss the development of a smartphone-based epifluorescence microscope (SeFM) for imaging fresh tissue samples at subcellular resolution. Recently, researchers have developed a smartphone microscopy system for detecting norovirus copies in water

samples at a resolution of a single virus per microliter [13]. Furthermore, [14] describes a SFM for the imaging and identification of fluorescently labelled pathogenic bacteria. Additionally, the design and working of a SFM employing an optofluidic lens for the quantification of glucose is discussed in [15]. In the past, our group has also designed and manufactured SFMs which we demonstrated for imaging and quantification of fluorescent particles such as micro beads or fluorescently tagged leukocytes [16-18].

Though many SFM designs have been presented for microparticle imaging by the research community to date, there exists a lack of unique SFM designs capable of directly imaging and quantifying sub-micron specimens. For example, one such research, discussed in [19] describes the design and working of a SFM which can be used to image nanoparticles and single virus cells. Systems presented (not capable of fluorescent microscopy) in other studies shown in [20] and [21] describe the use of a ball lens for the construction of smartphone-based microscopes for sub-micron resolution. Although high resolution, utility of the ball lens resulted in image distortion and low field of views for imaging. Ability of directly imaging features/specimens in the sub-micron and nanometer range using portable SFM's will open up many possibilities and applications. Further enhancement of current SFM designs for enabling and improving submicron imaging requires a deep understanding of the various SFM functional blocks and their intricate relationships with the overall imaging performance.

In this paper, we explore different excitation modalities integrated within our 3D printed SFM on its imaging performance and it impacts to image micron/ sun-micron specimens and test targets. By varying spatial position of the excitation source, three variants of an SFM were created. In first variant the excitation source and the sample plane were aligned parallel to each other; in the second one, they were placed perpendicular to each other; and in the third one they were placed at an oblique angle. Green-fluorescent beads of different sizes (8.3, 2, 1, 0.8 μm) were imaged using each of these variants at a range of excitation voltage intensities to identify the optimal imaging parameters for each SFM design variant. Schematics for the three excitations modalities utilized in our SFM design variations along with a representative image showcasing the different types of noises observed in the captured fluorescent images is shown in Fig. 1.

Signal difference to noise ratio (SDNR) and contrast to noise ratio (CNR) parameters were then computed for the images obtained through the three SFM variants for performance evaluation [22-25]. We showcase our results and draw inferences to further improve the performance of upcoming SFMs and help us image even smaller test specimens and analytes.
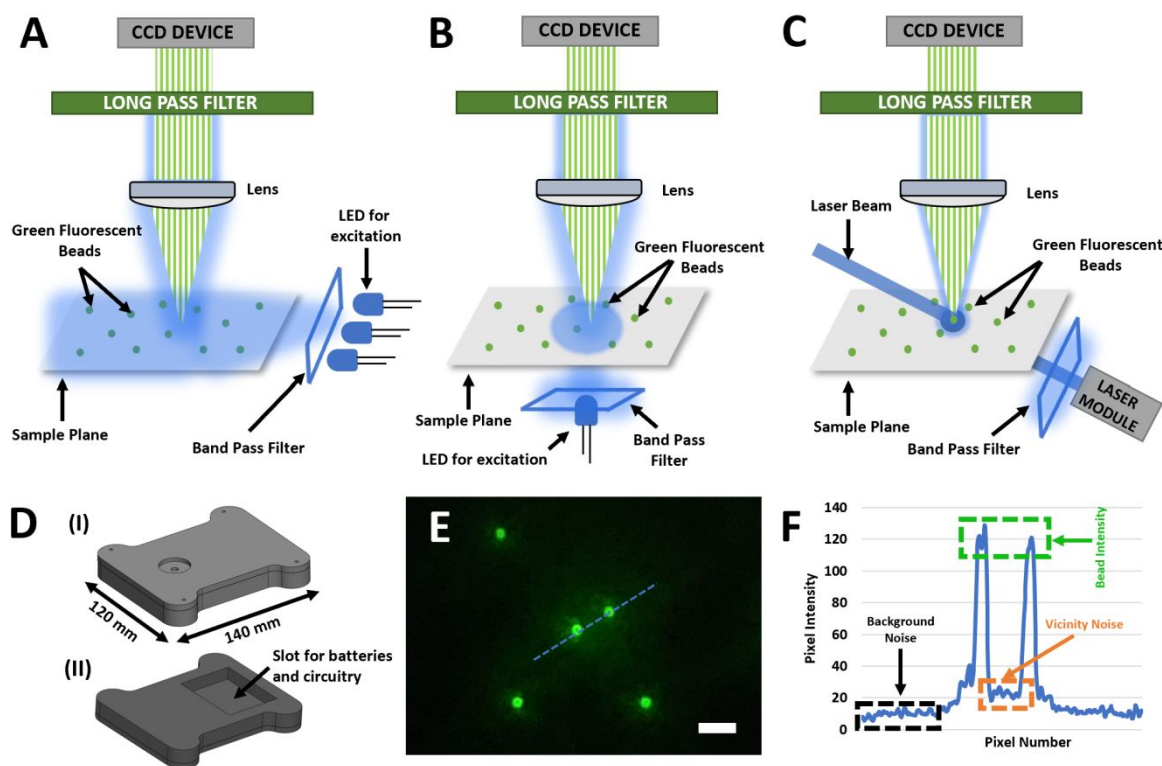
Figure 1: (a) Representative diagram for parallel excitation methodology in a Smartphone based fluorescent microscope. (b) Representative diagram for perpendicular excitation methodology in a Smartphone based fluorescent microscope. (c) Representative diagram for oblique excitation methodology in a Smartphone based fluorescent microscope. (d) CAD diagrams showcasing the dorsal and ventral sides of the designed SFM. (e) 8 μm green-fluorescent beads imaged from the smartphone attachment (Scale bar = 32μm). (f) Pixel intensity of the blue line drawn in Fig.1E showcasing the bead intensity, noise in the immediate vicinity of beads, and the background noise of the captured image.

2. Materials and Methods

2.1. Design of smartphone based fluorescent microscope

Excitation source is one of the primary building blocks in any SFM and therefore, holds immense importance. By changing the position of excitation source with respect to the sample plane, three excitation modality variants were created. The representative designs of these excitation modalities are showcased in

Fig. 1A, Fig.1B, and Fig. 1C. These excitation schemes were then used to develop three design variants for our SFM. These SFM systems were consisted of two parts, a top portion, and a bottom portion as shown in Fig. 1D.

The top portion is placed on top of the bottom portion, and it contains slots for an external lens, long pass filter, and four screws which can be rotated for manually adjusting the depth of focus. The external lens used for creating the magnification was procured from Edmund optics (Stock #87-165) and had a focal length of 3.1 mm. This lens worked in conjunction with the internal lens of the smartphone camera (Samsung Galaxy S21 Ultra) by forming a relay lens system and provided the magnification necessary for imaging. On top of the lens, a long pass filter with a cut-off value of 500 nm (Semrock, Product no: FF01-500/LP-23.3-D) is placed and it stops the blue light emitted from the excitation source to enter the camera module and only allows green light from the fluorescent sample to pass. All three SFM design variants shared the same design and configuration of the top portion. The detailed CAD layout for the top portions for each design variant can be seen in Fig. 2, Fig. 3, and Fig. 4 in the sections ahead.

The bottom portion of the designed SFM is used for housing the imaging sample, the excitation source (LED/laser module), and the electronic circuit. The exact design and specifications of the three design variants of the bottom portion are discussed individually as detailed below.

2.1.1. Parallel excitation modality

In parallel excitation, the excitation source is placed parallel to the sample plane as shown in Fig. 1A. The computer-aided design (CAD) layout for SFM using a parallel excitation modality and its associated imaging results are shown in Fig. 2. The bottom portion employing a parallel excitation modality has two cavities, one for the placement of circuits and excitation source and the other cavity for the placement of the sample for imaging (Fig. 2A). Furthermore, the bottom portion also has an opening for the placement of LED's (parallel to the sample plane) which are used for exciting the sample under consideration. Three blue LED's (Product no: 516-2800-1-ND) were purchased from Digi Key corporation and connected in parallel for the purpose of sample excitation. A bandpass filter with a centre wavelength of 470 nm and

bandwidth of ~40 nm (Chroma Inc, Product no. ET470/40x) was placed in front of the three LEDs to only allow blue light to enter imaging chamber. A cover shield was used to cover the imaging sample placed in the imaging cavity and helped in achieving the required darkfield by keeping unwanted blue light from getting through to the smartphone's camera sensor. Black electrical insulation tape was used to cover the inside of the SFM for absorbing unwanted excitation photons and to further help in creation of the darkfield for fluorescent imaging. The excited sample is then imaged using a smartphone which works in conjunction with the lens and the long pass filter of the top portion. Each fluorescent particle sample was imaged at excitation voltages ranging from a minimum of 3.1V to a maximum of 3.6V with a step size of 0.1V.

2.1.2. Perpendicular excitation modality

In perpendicular excitation, the excitation source is placed perpendicular (directly underneath) to the sample plane as shown in Fig. 1B. The CAD layout for the SFM employing a perpendicular excitation modality and its associated results are shown in Fig. 3. As shown in Fig. 3A, bottom portion employing a perpendicular excitation modality contains an extra part for holding the excitation source (LED). The CAD design of the LED holder is shown in Fig. S1. A single blue LED (Product no: 516-2800-1-ND) from Digi-Key is placed inside the LED holder and a bandpass filter with a centre wavelength of 470 nm and bandwidth of ~40 nm (Chroma Inc, Product no. ET470/40x) is placed in the bandpass filter slot as shown in Fig. S1. The sample to be imaged is then placed directly on top of the bandpass filter which gets excited from the LED which is directly underneath it and placed inside the LED holder. No cover shield is needed in case of a perpendicular excitation modality because of the small size of the opening in the LED holder as seen in Fig. S1. Black electrical insulation tape was used to cover the LED holder, bandpass filter, and the insides of the SFM for absorbing unwanted excitation photons and to further help in creation of the darkfield for fluorescent imaging. The excited sample is imaged using a smartphone which works in conjunction with the lens and the long pass filter of the top portion. Each fluorescent particle sample was imaged at excitation voltages ranging from a minimum of 2.4V to a maximum of 3.0V with a step size of 0.1V.

2.1.3. Oblique excitation modality

In oblique excitation, the excitation source is placed at an oblique angle to the sample plane as shown in Fig. 1C. The CAD layout for the SFM employing an oblique excitation modality and its associated results are shown in Fig. 4. As evident from Fig. 4A, the bottom portion with oblique excitation is significantly different as compared to the bottom portions used for parallel and perpendicular excitation modalities. Rather than employing LEDs, here, a laser module is used as an excitation source. Instead of using an off the shelf laser module, a customised laser module was designed while considering the needs and design constraints of our SFM. The design of the laser module employed in the oblique excitation modality can be seen in Fig. S1 and contains three parts, a blue laser diode, a lens for focusing the light emitted by the laser diode, and a 2 mm circular slit to get rid of any unfocused light. The laser diode was procured from mouser electronics (Mfr. #: PLT5 450B) and had an excitation wavelength of 450nm and a power rating of 80 mW. The lens used for focusing the light emitted by the laser diode was procured from Edmund optics (Stock #45-208) and had a focal length of 10 mm.

From Fig. 4A, we can see that the light beam coming from the laser module passes through a bandpass filter with a centre wavelength of 470 nm and bandwidth of ~40 nm (Chroma Inc, Product no. ET470/40x) and excites the sample placed in the sample placement slot at an oblique angle of 15° as shown in in Fig. 4A. A cover shield is used to cover the specimen that is being imaged and it helps in keeping any unwanted stray blue light from getting through to the smartphone's camera sensor. The opening in the cover shield measures about 3 x 1mm and represents the effective area for laser excitation and particle imaging in SFM equipped with an oblique excitation scheme. Black electrical insulation tape was used to cover the inside of the SFM for absorbing unwanted excitation photons and to further help in creation of the darkfield for fluorescent imaging. This excited sample is then imaged using a smartphone which works in conjunction with the lens and the long pass filter of the top portion. Each fluorescent particle sample was imaged at excitation voltages ranging from a minimum of 3.8V to a maximum of 4.5V with a step size of 0.1V.

2.2.   Fabrication of the SFM variants

The designed SFM and all its variants were 3D printed to conduct experiments. To do so, Mark Two 3D printer from Markforged was used and the printing was done using onyx thermoplastic material. Fig. S2 shows a 3D printed prototype of the SFM working in conjunction with a Samsung Galaxy S21 Ultra.

2.3.   Optical resolution measurement

A 1951 USAF resolution test chart from Edmund optics (Catalog # R1DS1P) was used to quantify the optical resolution of the designed microscopic smartphone attachment. Samsung Galaxy S21 Ultra was used in conjunction with the external 3.1 mm focal length lens to image the resolution test chart. ImageJ was then used to look at the pixel intensities of the different targets present in the resolution test chart. A target on the test chart was deemed resolvable only if its corresponding pixel intensity peaks obtained using ImageJ were clearly distinguishable from each other.

2.4.   Sample preparation for green-fluorescent beads

Green-fluorescent beads of four different sizes (8.3 µm, 2.0 µm, 1.0 µm, and 0.8 µm) were imaged using the three variants of the SFM. Bangs laboratories was used to procure 8.3 µm (Product # UMDG003), 2.0 µm (Product # FSDG005), and 1.0 µm (Product # FSDG004) green-fluorescent beads whereas 0.8 µm beads were procured from Spherotech (product number: HFP-0852-5). Different concentrations of these fluorescent beads were prepared by diluting them in 1X PBS from ThermoFisher Scientific (Catalog number: 20012050). Afterwards, 1µl of each bead sample was imaged using the three variants of the SFM based on their respective excitation voltage ranges. Furthermore, all experiments were done in triplicates so that the obtained results could be verified and the relative differences among the data could be measured and compared.

2.5.   Image acquisition protocol on Smartphone

A Samsung Galaxy S21 Ultra was used to image the green-fluorescent beads on the three variants of the SFM. For making the imaging process simpler and uniform across the study, all images were captured in

the auto mode of the smartphone built-in camera app and therefore, the imaging parameters (white balance, exposure time, focus mode etc) were auto-selected while capturing an image. This is to ensure robustness and ease of the user. Furthermore, a digital zoom of 6X was applied in all the captured images.

2.6. Determination of optimal excitation voltage range

Each design variant of the SFM was used to image the fluorescent bead samples at multiple excitation voltages. By juxtaposing the obtained images for a particular sample, we were able to identify three distinct regions in the excitation voltage range. There is an optimal region in which no data loss occurs, and background noise is low or within an acceptable level. Voltage levels below this optimal region constitute the data loss region and the voltage levels above the optimal range constitute the high noise region. Protocols used for the identification of the data loss and high noise regions for each SFM design variant are discussed below:

2.6.1. Data loss region

We wanted to identify the threshold of excitation voltage below which data loss starts to occur and some beads are not imaged. For this quality control, ImageJ was used to quantify the number of beads in the images obtained at each respective excitation voltage. Analysing the obtained counts allowed us to identify the threshold of excitation voltage below which some beads are not imaged, and data loss started to occur.

2.6.2. High noise region

Quantifying the minimum excitation voltage required to successfully image all beads present in the sample is critical. If excitation voltage is kept on increasing, it results in an increase in the noise of the obtained fluorescent image as well by reducing the quality of the darkfield obtained. The point where the quality of the darkfield image obtained significantly deteriorates or the bead vicinity noise is at an unacceptable level, constitutes the lower bound of the high noise region. These voltage thresholds were determined by visually accessing the quality of captured images.

2.7. SDNR and CNR calculation

After identifying the optimal excitation voltage range for each particle size in the three variants of the SFM, we further analysed the images obtained in the optimal excitation voltage range. Using ImageJ, we quantified the intensity of an imaged bead, the intensity of the noise in bead vicinity, and the overall background noise of the image. Fig. 1E shows 8.3 µm green-fluorescent beads imaged using the perpendicular excitation modality and the corresponding Fig. 1F shows the pixel intensity of the beads, vicinity noise, and the background noise. Using these three parameters we calculated the signal difference to noise ratio (SDNR) and contrast to noise ratio (CNR) for a single bead based on the equations 1, 2, and 3 [22-25].

$$SDNR = \frac{Bead\ Intensity - Viccinity\ Noise}{Background\ Noise} \tag{1}$$

$$Contrast = \frac{Bead\ Intensity - Viccinity\ Noise}{Viccinity\ Noise} \tag{2}$$

$$CNR = \frac{Contrast}{Background\ Noise} \tag{3}$$

The SDNR and CNR values for one complete image were calculated by taking an average of the SDNR and CNR of ten beads present in that respective image. To select these ten beads, the image was first divided into three regions and then a diagonal was drawn from the bottom left corner to the top right corner as shown in Fig. S3. Three beads each from regions 1 and 3 and four beads from region 2 that were close to the diagonal were picked for calculation of their respective SDNR and CNR values. In case if there were less than required beads present in any region, more beads from other regions were picked to make up for the loss.

3. Results

3.1.   Optical resolution

Samsung Galaxy S21 Ultra was used in conjunction with the SFM for fluorescent imaging. The camera module of S21 Ultra has an internal lens with a focal length of 6.7 mm which works in conjunction with the 3.1 mm external lens of the SFM to form a relay lens system. Based on the focal lengths of the two lenses involved, a magnification factor of 2.16 was achieved. A USAF chart was used to quantify the obtained optical resolution. Fig. S4 shows the imaged 1951 USAF test chart along with the pixel intensities of Group 7 Element 6 which point towards an optical resolution of 2.2 μm. Group 7 Element 6, is the smallest feature size element available on the USAF chart we used.

3.2.   Smartphone based fluorescent microscope variants

The designed SFM variants were used to image fluorescent particles of sizes 8.3, 2, 1, and 0.8 μm. The imaging performance of the three variants is discussed individually below.

3.2.1. *Parallel excitation modality*

In parallel excitation scheme, the excitation source (LEDs) is placed parallel to the sample plane. As mentioned previously, all four bead sizes were imaged at excitation voltages ranging from 3.1 V to 3.6 V with a step size of 0.1 V. This variant of the SFM was only able to image the 8.3 μm beads as shown in Fig. 2B. When smaller sized fluorescent particles were imaged using this variant of the SFM, we were not able to see and discern them. The images obtained for 2 μm, 1 μm, and 0.8 μm beads using this variant of the SFM are shown in Fig. 2C, Fig. 2D, and Fig. 2E respectively.
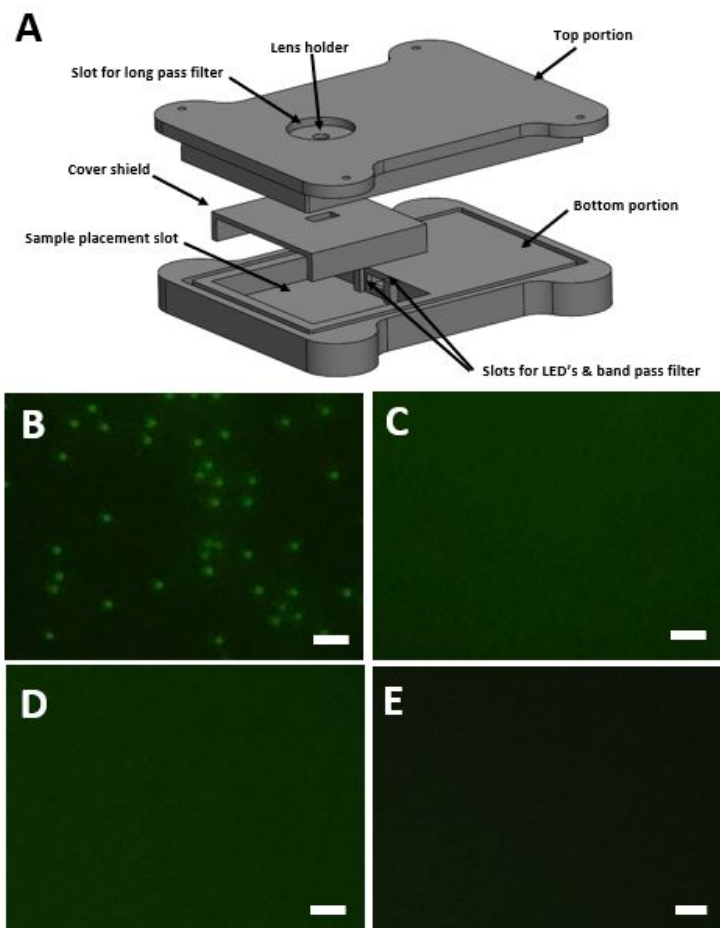
Figure 2: (a) Disbanded 3D CAD model of the designed microscopic smartphone attachment with a parallel excitation scheme. (b) 8.3 μm green-fluorescent particles imaged from the smartphone attachment using parallel excitation at 3.1 V. (c) 2 μm green-fluorescent particles imaged from the smartphone attachment using parallel excitation at 3.6 V (d) 1 μm green-fluorescent particles imaged from the smartphone attachment using parallel excitation at 3.6 V(e) 0.8 μm green-fluorescent particles imaged from the smartphone attachment using parallel excitation at 3.6 V. (Scale bar = 32μm)

3.2.2. *Perpendicular excitation modality*

In the perpendicular excitation scheme, the excitation source (LED) is placed perpendicular to the sample plane. Similar to previous protocol, all four bead sizes (8.3, 2, 1, and 0.8 μm) were imaged. The excitation voltage range used was between 2.4 V and 3.0 V with a step size of 0.1 V. This variant of the SFM was able to successfully image all the four bead sizes. Fig. 3B shows the representative image obtained for 8.3 μm beads and similarly Fig. 3C, Fig. 3D, and Fig. 3E showcase the images obtained for 2, 1, and 0.8 μm fluorescent beads respectively.
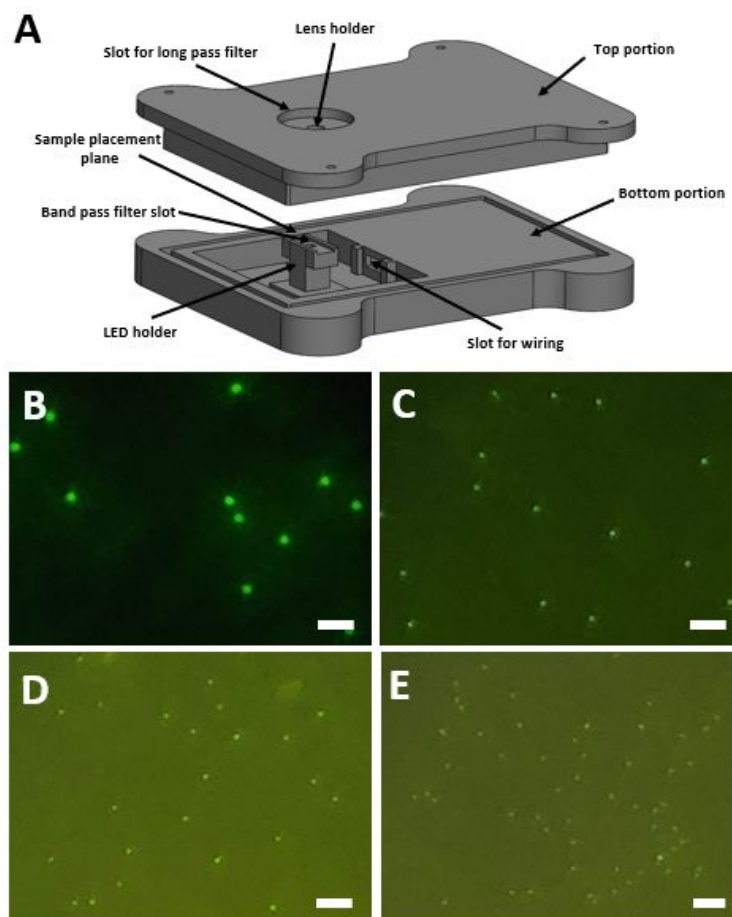
Figure 3: (a) Disbanded 3D CAD model of the designed microscopic smartphone attachment with a perpendicular excitation modality. (b) 8.3 μm green-fluorescent particles imaged from the smartphone attachment using perpendicular excitation at 2.4 V. (c) 2 μm green-fluorescent particles imaged from the smartphone attachment using perpendicular excitation at 2.6 V. (d) 1 μm green-fluorescent particles imaged from the smartphone attachment using perpendicular excitation at 2.8 V. (e) 0.8 μm green-fluorescent particles imaged from the smartphone attachment using perpendicular excitation at 2.8 V. (Scale bar = 32μm).

3.2.3. *Oblique excitation modality*

In oblique excitation scheme, the excitation source (laser module) is placed at an oblique angle of 15° to

the sample plane. Here, all four bead sizes (8.3, 2, 1, and 0.8 μm) were imaged at excitation voltages ranging

from 3.8 V to 4.5 V with a step size of 0.1 V. This variant of the SFM was successfully able to image the

four bead sizes too. Fig. 4B shows the representative image obtained for 8.3 μm beads and similarly Fig.

4C, Fig. 4D, and Fig. 4E showcase the images obtained for 2, 1, and 0.8 μm fluorescent beads respectively.
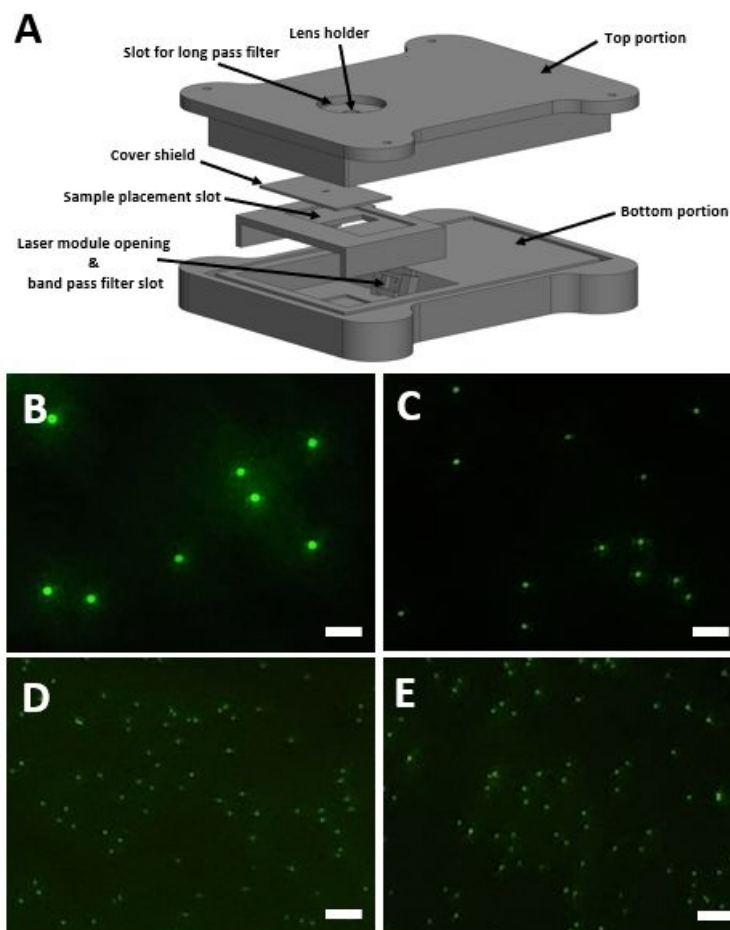
Figure 4: (a) Disbanded 3D CAD model of the designed microscopic smartphone attachment with an oblique excitation modality. (b) 8.3 µm green-fluorescent particles imaged from the smartphone attachment using an oblique excitation modality at 3.8 V. (c) 2 µm green-fluorescent particles imaged from the smartphone attachment using an oblique excitation modality at 4.1 V. (d) 1 µm green-fluorescent particles imaged from the smartphone attachment using oblique excitation modality at 4.3 V. (e) 0.8 µm green-fluorescent particles imaged from the smartphone attachment using oblique excitation modality at 4.3 V. (Scale bar = 32µm).

3.3. Optimal excitation voltage range

The optimal excitation voltage range for the four particles was found for each design variant of the SFM

using the methodology described earlier. The results obtained for each design variant are enlisted in the

subsections below.

3.3.1. *Parallel excitation modality*

The SFM variant employing parallel excitation modality was only able to image the 8.3 μm fluorescent

beads and not the smaller ones. Bead quantification using ImageJ revealed that no data loss region existed

for the 8.3 μm beads as the number of beads imaged at each excitation voltage were similar in numbers.

Similarly, no high noise region could be identified as the noise present in the captured images (even at the

highest excitation voltage we used) was reasonable and did not warrant inclusion in the high noise region.

Fig. 5 below shows the bead count for the 8.3 μm beads in the entire excitation range along with some

representations of the beads imaged at different excitation intensities.
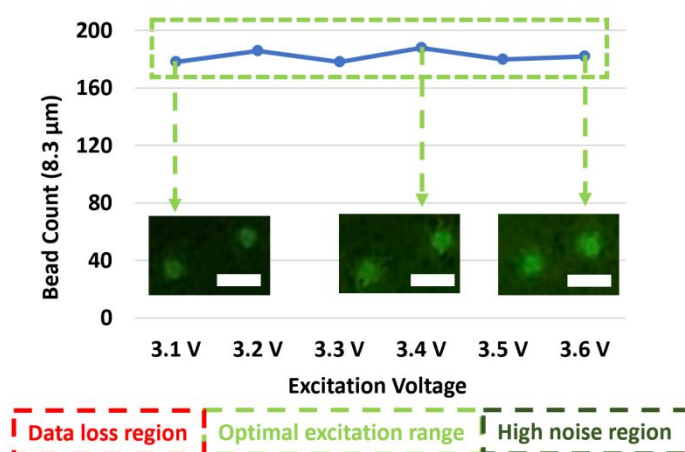
Figure 5: Bead counts, bead images, and delineated excitation voltage regions for the 8.3 μm fluorescent
beads imaged using the SFM employing a parallel excitation scheme (Scale bar = 15 μm).

3.3.2. *Perpendicular excitation modality*

The SFM variant employing perpendicular excitation modality was successfully able to image all the four

fluorescent beads. Bead counts, bead images, and delineated excitation voltage regions for the 8.3 μm

beads are shown in Fig. 6A. For 8.3 μm beads, no data loss region existed but the images obtained above

2.4 V had a lot of noise and were thus included in the high noise region. Fig. 6B shows the bead counts,

bead images, and delineated excitation voltage regions for the 2 μm beads. Excitation voltages below 2.6

V constituted the data loss region and excitation voltages above 2.7 V made up the high noise region with

the optimal excitation voltage range sandwiched between the two of them as evident from Fig. 6B.

Similarly, Fig. 6C shows the bead counts, bead images, and delineated excitation voltage regions for the 1 μm beads. Excitation voltages below 2.8 V constituted the data loss region and the ones above it constituted the optimal excitation range. No high noise region was identified for 1 μm beads. Lastly, Fig. 6D shows the bead counts, bead images, and delineated excitation voltage regions for the 0.8 μm beads. Excitation voltages below 2.8 V constituted the data loss region and the ones above it constituted the optimal excitation range. No high noise region was identified for 0.8 μm beads as well.
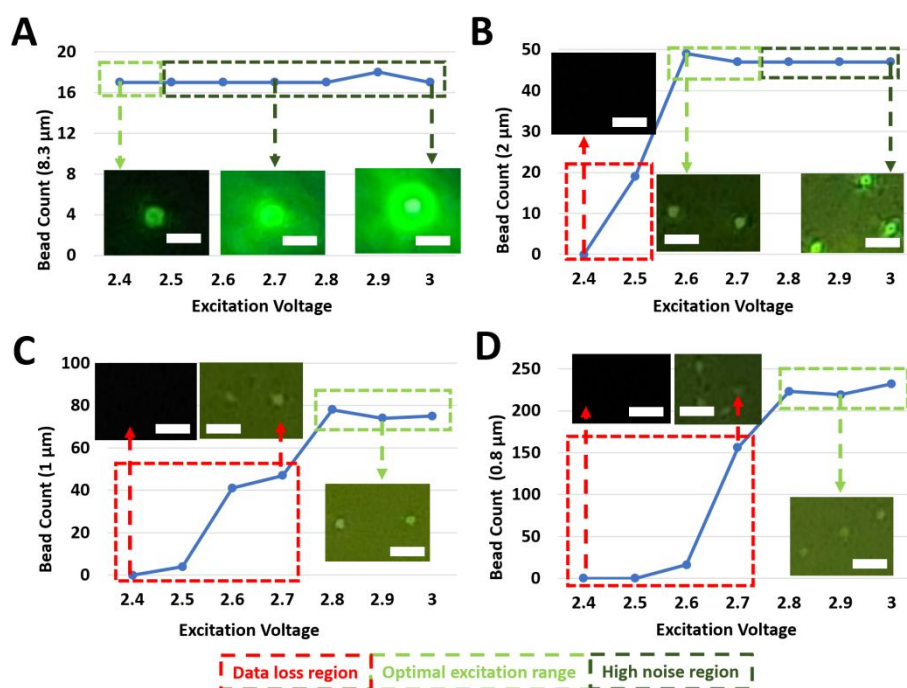
Figure 6: (a) Bead counts, bead images, and delineated excitation voltage regions for 8.3 μm fluorescent beads imaged using the SFM employing a perpendicular excitation scheme (Scale bar = 15 μm). (b) Bead counts, bead images, and delineated excitation voltage regions for 2 μm fluorescent beads imaged using the SFM employing a perpendicular excitation scheme (Scale bar = 5 μm). (c) Bead counts, bead images, and delineated excitation voltage regions for 1 μm fluorescent beads imaged using the SFM employing a perpendicular excitation scheme (Scale bar = 3 μm). (d) Bead counts, bead images, and delineated excitation voltage regions for 0.8 μm fluorescent beads imaged using the SFM employing a perpendicular excitation scheme (Scale bar = 3 μm).

3.3.3. *Oblique excitation modality*

The BFM variant employing an oblique excitation modality was successfully able to image all the four fluorescent beads. Bead counts, bead images, and delineated excitation voltage regions for the 8.3 μm

beads are shown in Fig. 7A. For 8.3 μm beads, no data loss region existed but the images obtained above

3.8V had a lot of noise and were thus included in the high noise region. Fig. 7B shows the bead counts,

bead images, and delineated excitation voltage regions for the 2 μm beads. Excitation voltages below 4.1V

constituted the data loss region and excitation voltages above 4.3V made up the high noise region with the

optimal excitation voltage range sandwiched between the two. Similarly, Fig. 7C shows the bead counts,

bead images, and delineated excitation voltage regions for the 1 μm beads. Excitation voltages below 4.3V

constituted the data loss region and the ones above it constituted the optimal excitation range. No high noise

region was identified for 1 μm beads. Lastly, Fig. 7D shows the bead counts, bead images, and delineated

excitation voltage regions for the 0.8 μm beads. Excitation voltages below 4.3V constituted the data loss

region and the ones above it constituted the optimal excitation range. No high noise region was identified

for 0.8 μm beads as well.
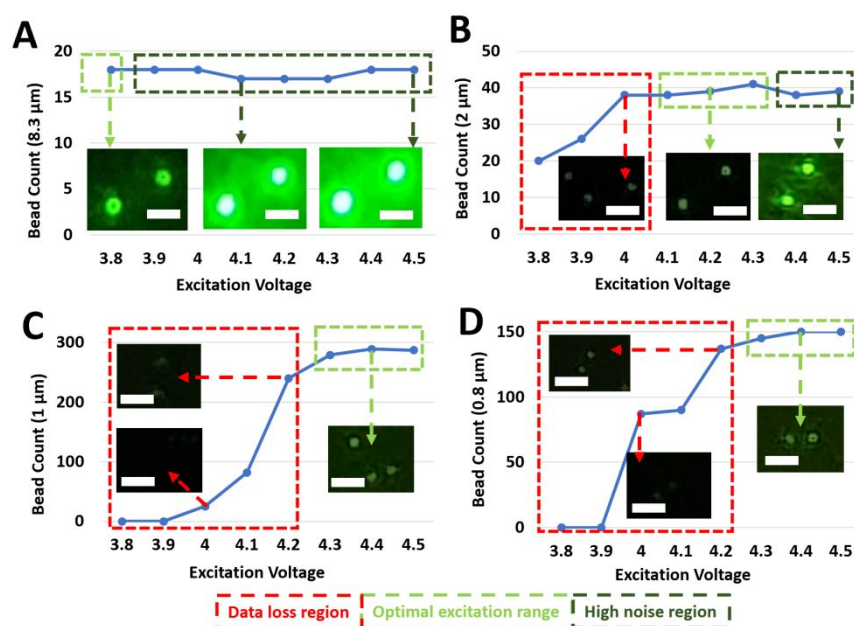
Figure 7: (a) Bead counts, bead images, and delineated excitation voltage regions for 8.3 μm fluorescent beads imaged using the SFM employing an oblique excitation scheme(Scale bar = 15 μm). (b) Bead counts, bead images, and delineated excitation voltage regions for 2 μm fluorescent beads imaged using the SFM employing an oblique excitation scheme (Scale bar = 5 μm). (c) Bead counts, bead images, and delineated excitation voltage regions for 1 μm fluorescent beads imaged using the SFM employing an oblique excitation scheme (Scale bar = 3 μm). (d) Bead counts, bead images, and delineated excitation voltage regions for 0.8 μm fluorescent beads imaged using the SFM employing an oblique excitation scheme (Scale bar = 5 μm).

3.4. SDNR and CNR

After the delineation of optimal excitation voltage ranges for the fluorescent particles in the three SFM variants, further performance analysis was carried out. SDNR and CNR for the bead images captured in the optimal excitation ranges were computed to get an idea about the relative imaging performance of the three SFM design variants. The results obtained for each design variant are discussed in the sections below.

3.4.1. *Parallel excitation modality*

The SFM variant employing a parallel excitation modality was only able to image the 8.3 μm fluorescent beads. An optimal excitation range of 3.1 to 3.6V was identified for these beads. The SDNR values of the 8.3 μm beads imaged in the optimal excitation range are shown in Fig. 8A and their corresponding CNR values are shown in Fig. 8B.
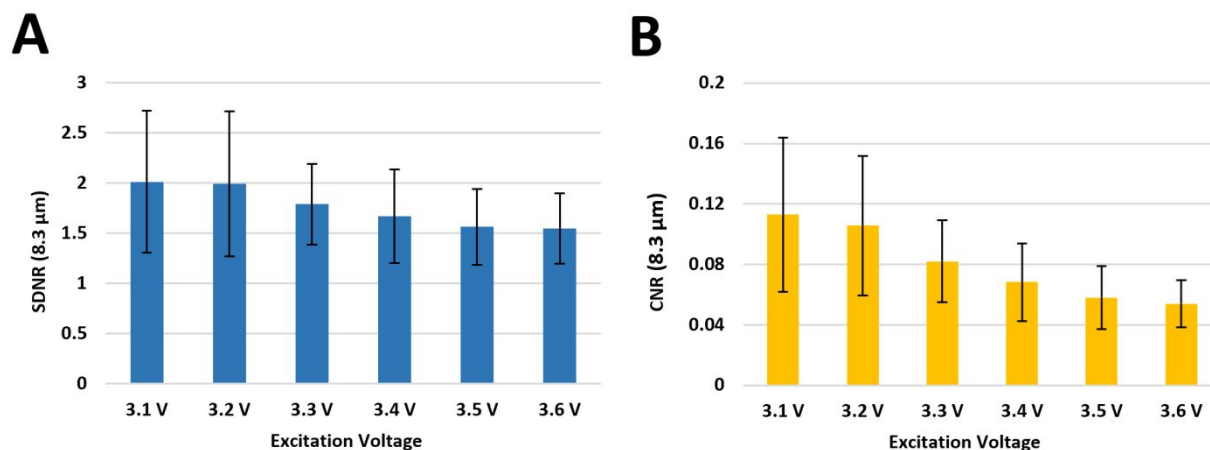
Figure 8: (a) SDNR values in optimal excitation voltage range for 8.3 μm fluorescent beads imaged using the SFM employing a parallel excitation scheme. (b) CNR values in optimal excitation voltage range for 8.3 μm fluorescent beads imaged using the SFM employing a parallel excitation scheme.

3.4.2. *Perpendicular excitation modality*

The SFM variant employing a perpendicular excitation modality was able to image all the four fluorescent beads (8.3, 2, 1, 0.8 μm). For 8.3 μm an optimal excitation voltage of 2.4V was identified. The SDNR value of the 8.3 μm beads imaged at the optimal excitation voltage is shown in Fig. 9A (I) and the corresponding CNR value is shown in Fig. 9A (II). For 2 μm beads an optimal excitation range of 2.6 to 2.7V was

identified. The SDNR values of the 2 µm beads imaged in the optimal excitation range are shown in Fig.9B (I) and the corresponding CNR values are shown in Fig. 9B (II). For 1 µm beads an optimal excitation range of 2.8 to 3.0V was identified. The SDNR values of the 1 µm beads imaged in the optimal excitation range are shown in Fig.9C (I) and the corresponding CNR values are shown in Fig. 9C (II). For 0.8 µm beads an optimal excitation range of 2.8 to 3.0V was identified. The SDNR values of the 0.8 µm beads imaged in the optimal excitation range are shown in Fig. 9D (I) and the corresponding CNR values are shown in Fig.9D (II).
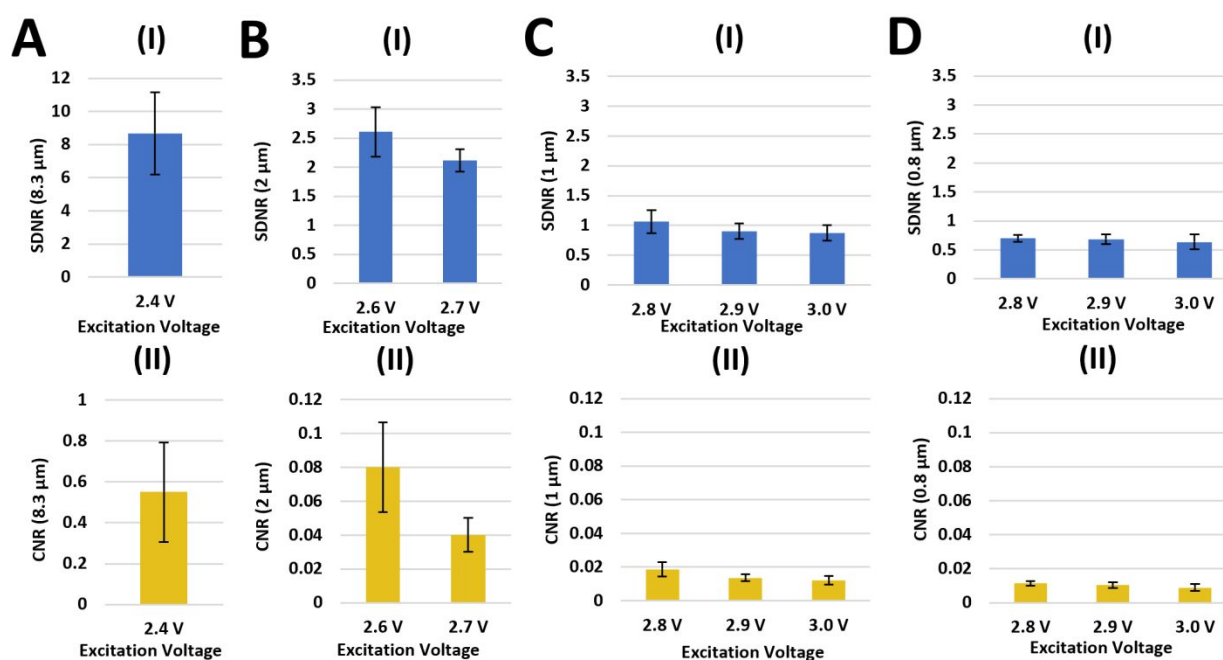
Figure 9: (a) (I) SDNR value at optimal excitation voltage for 8.3 µm fluorescent beads imaged using the SFM employing a perpendicular excitation scheme. (II) Corresponding CNR values. (b) (I) SDNR values in optimal excitation voltage for 2 µm fluorescent beads imaged using the SFM employing a perpendicular excitation scheme. (II) Corresponding CNR values. (C) (I) SDNR values in optimal excitation voltage for 1 µm fluorescent beads imaged using the SFM employing a perpendicular excitation scheme. (II) Corresponding CNR values. (d) (I) SDNR values in optimal excitation voltage for 0.8 µm fluorescent beads imaged using the SFM employing a perpendicular excitation scheme. (II) Corresponding CNR values.

3.4.3. *Oblique excitation modality*

The SFM variant employing an oblique excitation modality was able to image all the four fluorescent beads (8.3, 2, 1, 0.8 μm). For 8.3 μm an optimal excitation voltage of 3.8 V was identified. The SDNR value of the 8.3 μm beads imaged at the optimal excitation voltage is shown in Fig.10A (I) and the corresponding CNR value is shown in Fig. 10A (II). For 2 μm beads an optimal excitation range of 4.1 to 4.3V was identified. The SDNR values of the 2 μm beads imaged in the optimal excitation range are shown in Fig. 10B (I) and the corresponding CNR values are shown in Fig. 10B (II). For 1 μm beads an optimal excitation range of 4.3 to 4.5V was identified. The SDNR values of the 1 μm beads imaged in the optimal excitation range are shown in Fig. 10C (I) and the corresponding CNR values are shown in Fig. 10C (II). For 0.8 μm beads an optimal excitation range of 4.3 to 4.5V was identified. The SDNR values of the 0.8 μm beads imaged in the optimal excitation range are shown in Fig. 10D (I) and the corresponding CNR values are shown in Fig. 10D (II).
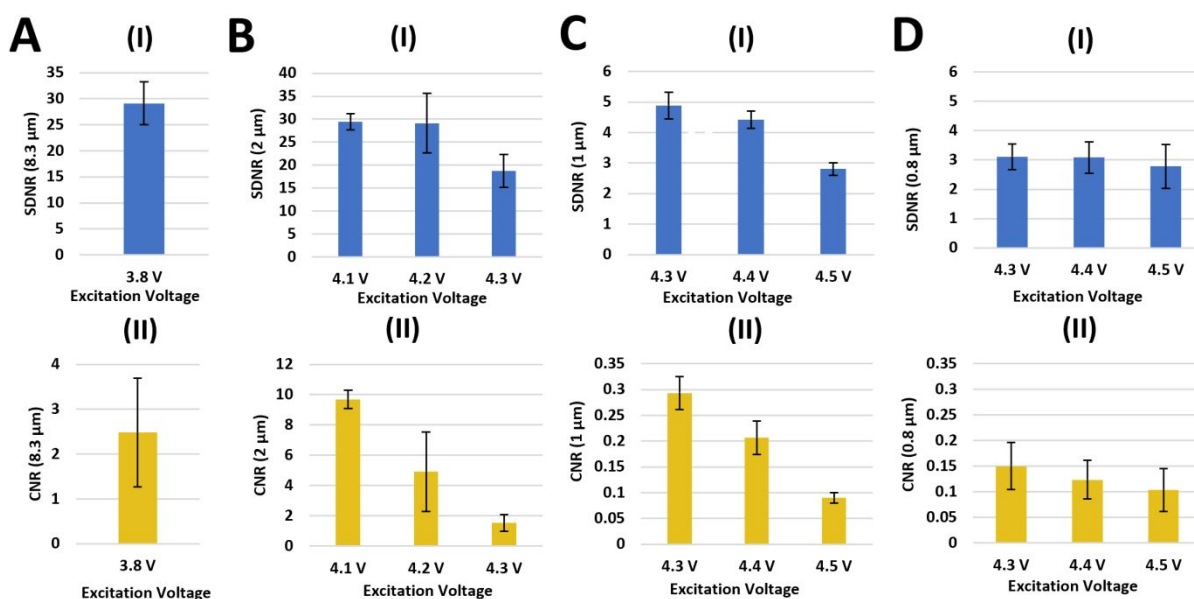
Figure 10: (a) (I) SDNR value at optimal excitation voltage for 8.3 μm fluorescent beads imaged using the SFM employing an oblique excitation scheme. (II) Corresponding CNR values. (b) (I) SDNR values in optimal excitation voltage for 2 μm fluorescent beads imaged using the SFM employing an oblique excitation scheme. (II) Corresponding CNR values. (C) (I) SDNR values in optimal excitation voltage for 1 μm fluorescent beads imaged using the SFM employing an oblique excitation scheme. (II) Corresponding CNR values. (d) (I) SDNR values in optimal excitation voltage for 0.8 μm fluorescent beads imaged using the SFM employing an oblique excitation scheme. (II) Corresponding CNR values.

4. Discussion

Spatial positional variations of the excitation source with respect to the sample plane allowed us to manufacture three variants of the SFM as shown in Fig. 1. Except excitation modality variation, the three design variants were completely identical and employed the same optical and imaging components for fluorescent imaging of four different green-fluorescent beads (8.3, 2, 1, 0.8 μm). Excitation sources for each SFM modality were chosen based on the unique design features and requirements of each modality. LEDs were selected as the excitation source for parallel excitation because of their high angular displacement which allows them to illuminate the entire sample imaging slot. For, perpendicular excitation, an LED is selected again to excite the fluorescent sample directly and closely while considering the limitations of the bandpass filter which is used to remove the unwanted light from the excitation source. Finally, a laser diode was picked for the oblique excitation scheme because a very focused light beam with minimal energy wastage is required considering angular displacement.

Fig. 2 showcases that the design variant employing a parallel excitation modality was able to image 8.3 μm beads successfully but not the smaller ones despite having adequate optical resolution. The suboptimal imaging performance of the SFM employing a parallel excitation modality can be attributed to the wastage of excitation light. Only a fraction of the light emitted from the excitation LEDs reaches the fluorescent beads while the rest of it is spread around the imaging chamber. This fraction of light reaching the beads on the sample plane is enough to excite and image the bigger 8.3 μm beads but not the smaller ones, limiting their imaging. In contrast, the SFM design variants employing perpendicular and oblique excitation modalities were successfully able to image all four bead sizes because the excitation light is more direct and is focused directly on the beads present on the sample plane, resulting in a higher energy delivery to the fluorescent particles as evident from the results shown in Figs. 3 and 4.

The green-fluorescent beads were imaged at multiple excitation voltages using the three SFM variants to identify the optimal excitation voltage range. As shown in Fig. 5, SFM with parallel excitation modality was only able to image 8.3 μm beads. The noise levels were also within the acceptable levels at all the

applied excitation voltages (3.1 to 3.6 V). Therefore, SFM with parallel excitation modality is shown to be quite robust for imaging 8.3 μm beads but is not suitable for imaging smaller sized and sub-micron beads. For SFMs equipped with perpendicular and oblique excitation schemes, the fluorescent beads were imaged at voltage levels ranging between 2.4 to 3.0 V and 3.8 to 4.5 V respectively, as shown in Figs. 6 and 7. The performance trend observed for the optical excitation region was quite similar in these two SFM variants. For the bigger 8.3 μm beads, no data loss region was observed but the application of higher excitation voltages resulted in an increase in the noise levels and thus constituted the high noise region. For 2 μm beads, we observe the presence of a data loss region at lower excitation voltages and the high noise region exists at higher excitation voltages with the optimal excitation range present between the two. For the smaller beads (1 and 0.8 μm), we observed the presence of a data loss region towards the lower excitation voltages and the optimal excitation region present towards the higher excitation voltages with the high noise region being completely absent.

Fig. S5 identifies the position of data loss, optimal, and high noise regions for the three SFM design variants. From Fig. S5 we can observe that as the bead size decreases, the minimum excitation voltage required to successfully image the bead goes higher. This validates our earlier hypothesis that SFM with a parallel excitation modality fails to image the smaller fluorescent particles. Another interesting thing to note is the presence of high noise regions only with the bigger 8.3 and 2 μm beads and not with the smaller 1 and 0.8 μm beads, even when imaged at the highest excitation voltage for any particular variant as shown in Figs. 6 and 7. Based on this observation, we can infer that the high noise region is more heavily influenced by the vicinity noise from the beads being imaged compared to the background noise of the image which is dependent on the noise present in the excitation source (LED/Laser diode).

Fig. S6 showcases the lower end of the optimal excitation range for the four bead sizes (8.3,2,1,0.8 μm) imaged using the perpendicular and oblique excitation variants of the SFM. It can be observed that to image smaller beads, the minimum required excitation voltage increases. However, depending on the SFM design,

increasing the excitation voltage beyond a certain threshold would result in transitioning to the high noise region as shown in Figs 5, 6, and 7.

In addition to identifying the relative positions of data lass, optimal, and high noise regions, it is also important to discuss the reasons behind such performance. Data loss region occurs when the excitation energy being delivered by the excitation source (LED/Laser diode) is not enough to successfully excite the fluorescent particles so that they can be imaged by the charged-coupled device (CCD) sensor. This is evident as the data loss region exists towards the lower end of the voltage spectrum. To shift from data loss region to optimal excitation region, the intensity of the excitation source needs to be increased which results in increased intensity of the particle fluorescence output. A further increase in the excitation source will result in shift to into the high noise region where fluorescent particles though fluoresce with a higher intensity but are accompanied by an undesired increase in both the background and the vicinity noise. Transitioning between data loss, optimal, and high noise region by increasing the intensity of excitation source is illustrated, for example, by the results obtained when 2 μm beads were imaged using SFM with perpendicular and oblique excitation schemes as shown in Figs. 6 and 7. 2 μm beads are the only ones to display all three regions (data loss, optimal, and high noise) and transitioning in between regions resulted by increasing intensity of excitation source, thus confirming the explanations provided above.

We also compared and quantified the quality of the images obtained from each SFM variant in its optimal excitation voltage range. This was done using two success metrics, the contrast to noise ratio (CNR) and the signal difference to noise ratio (SDNR) [22-25]. The ability to distinguish between two regions is directly related to their contrast and inversely related to the background noise, highlighting the need to use CNR to measure the contrast generating ability in the SFM variants. Additionally, CNR also has a limitation that it is display dependent, therefore, we also measured the SDNR for each image captured in the optimal excitation regions as it is a display independent parameter [22-25].

The SDNR/CNR values for the three SFM design variants are shown in Figs. 8, 9, and 10. In all three variants, the highest SDNR/CNR value for all four beads (8.3, 2, 1, 0.8 μm) occur at the lowest voltage of

their respective optimal excitation range. This is because increasing the excitation voltage also increases the image background noise, which being in denominator for both SDNR and CNR, reduces their overall values. The corresponding values for bead and vicinity noise intensity of the SFM variants are shown in Figs. S7, S8, and S9. As expected, an increase in the intensity of the excitation source results in an increase in both the bead intensity and the vicinity noise.

It is interesting to note in Fig. 9 and 10, that the SDNR/CNR values obtained in both SFM design variants for the bigger 8.3 and 2 μm beads are significantly higher compared to the 1 and 0.8 μm beads. There are two possible reasons for this occurrence. First, the surface of bigger beads contains more fluorophores which results in a higher fluorescent intensity for these beads compared to smaller ones. Since the bead fluorescent intensity is directly related to SDNR/CNR, we get higher values for the bigger beads. Secondly, the optimal excitation voltage range of the smaller beads is higher compared to the bigger beads in all SFM variants. Higher excitation intensity results in an increase in the background noise of the image. This background noise is inversely related to both CNR and SDNR which further reduces their value.

Furthermore, as seen from Figs. 9 and 10, the SDNR/CNR values obtained from the SFM variant with an oblique excitation modality are also significantly higher compared to the ones obtained from the variant employing a perpendicular excitation modality even though the average bead intensities obtained using the two variants are similar as seen from Figs. S8 and S9. This difference between the performance of the two variants can be attributed to the extremely high image background noise present in the images captured using perpendicular excitation variant. The excitation source (LED) in the perpendicular variant is placed directly underneath the sample plane and it is directly in line with the CCD sensor. Other than the required blue light, this LED also emits a portion of green light as well whose magnitude at higher excitation voltage levels becomes too strong for the band pass filter placed directly ahead of it. This unwanted green light then manifests itself as a very strong image background noise, thereby reducing the performance of perpendicular excitation variant.

It is also important to notice the behaviour of the error bars associated with the SDNR/CNR values depicted in Figs. 8, 9, and 10. We can notice the presence of relatively large error bars especially at lower excitation voltages. The behaviour of error bars observed in Figs. 8, 9, and 10 is due to the mathematical nature of SDNR and CNR functions. Both SDNR and CNR have the background noise component in the denominator. At lower excitation voltages, background noise is also low which gives us higher SDNR/CNR values but small variations in these already low background noise values correspond to a much higher change in the calculated SDNR/CNR value and thus increases the standard deviation. At higher excitation voltages, background noise is comparatively higher which is why slight variation in its value do not have a very dramatic effect on the calculated SDNR /CNR standard deviation.

We found some interesting novel observations regarding existence of unique intensity profiles in the captured images. These can be classified into four different types based on the unique features of background and bead vicinity noises as shown in Fig. S10. In the first type, there exists very low background noise as depicted by the near perfect darkfield. The bead vicinity noise appears in a smooth and uniform way and is limited to the immediate neighbourhood of the imaged beads. This type was observed in all three design variants when the bigger 8.3 and 2 μm beads were imaged at the middle or higher end of their respective optimal excitation voltage range (Figs. S10 A and B). In the second type, the image background noise is very high and superimposes itself over the bead vicinity noise. This makes it impossible to discern between the two and they have similar mean pixel intensity. This type was mainly observed when smaller 1 and 0.8 μm beads were imaged using an SFM with a perpendicular excitation modality (Figs. S10 C and D). In the third type, background noise level is acceptable with the vicinity noise appearing in the form of circular rings around the beads. This type was mainly observed when the smaller 1 and 0.8 μm beads were imaged using the SFM with an oblique excitation modality (Figs. S10 E and F). The fourth type can be referred to as the ideal performance for fluorescent imaging setup. Both the background and the bead vicinity noise levels negligible which results in very sharp and crisp images. This type was mainly observed with the bigger 8.3 and 2 μm beads when they were imaged using the SFM with an oblique excitation

modality at the lowest possible excitation level of their respective optimal excitation voltage range (Figs. S10 G and H). Naturally, this type of images had the best SDNR/CNR values because of extremely low noise levels.

The power consumption of the three SFM variants was also quantified by noting the current drawn from the power source. Tables S1, S2, and S3 list the current drawn by SFM variants in their complete respective voltage range. SFM with an oblique excitation modality required the most power while the one with a perpendicular excitation modality required the least power. This is expected as the power requirement for the laser diode are much higher compared to those of a single standalone LED. Furthermore, in Tables S4 and S5, we have provided the relative luminous intensity and optical power respectively of the excitation sources employed in the SFM with parallel and oblique excitation schemes. To replicate this study, similar excitation sources, setups, and imaging conditions must be used. Excitation sources with different specifications may result in different absolute numerical values as reported here, however the general performance trends would remain the same.

In Table S6, we have summarized all the parameters for the best images captured for all four bead sizes (8.3, 2, 1, 0.8 μm) by each SFM design variants. The SFM with an oblique excitation modality outperforms the other two but at the cost of significantly high-power consumption. If power conservation is a top priority and some concessions can be made on image background noise, a perpendicular excitation modality can be adopted because of its extremely low power requirements. Table S7 presents a relative comparison of the three SFM variants based on their imaging performance, field of view (FOV), and the required power. Fig. 11 depicts a general process flow model that can be referred to while choosing between the three SFM excitation modalities and Fig. S11 showcases a use case for this general process flow model depicting the choices to be made when 1 μm beads have to be imaged at highest possible SDNR/CNR values.
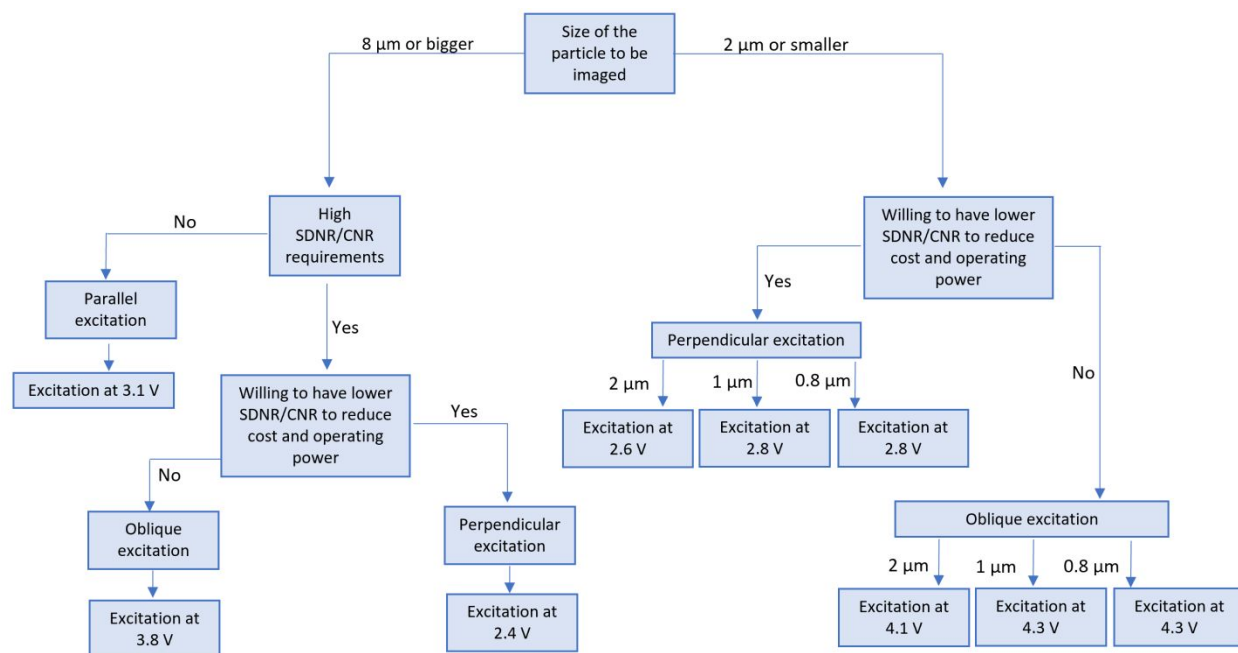
Fig 11. A general process flow model for choosing between the different excitation modalities of the SFM based on the user requirements and constraints.

The images collected in this study were captured using the auto mode of camera app. of Samsung Galaxy S21 Ultra. In the auto mode, the smartphone's processor automatically optimizes the camera parameters such as white balance, exposure time, and aperture size to capture the best possible image. This is in line with the translational goal of this study i.e., to enable the use of SFM by general public, therefore, utilizing auto mode is a better option as it eliminates the complexity of image capturing parameter selection by the user. Further, this study is focused on imaging fluorescent beads as it is a standard practice to use such particles for calibrating optical instruments because of their uniform brightness and photostability. The information obtained about calibrating the SFM variants and their performance can be used in future studies for the fluorescent imaging of pertinent biomarkers as well as bacterial/viral specimens for global health applications.

Author Contributions

M.S. participated in conceptualization, study design, writing original draft and preparing figures, data analysis. M. T. participated in data analysis, SDNR/CNR calculations, figures, and paper

review. U.H. participated in conceptualization, study design, funding acquisition, investigation, project administration, resources, supervision, writing – review & editing.

Conflicts of Interest

Authors declare no conflicts of interest.

Acknowledgements

Data Availability Statement

Data related to this study will be available upon request based on the funding agencies and Rutgers, The State University of New Jersey policies.

References

[1] R. Yuste, Fluorescence microscopy today, Nature Methods. 2 (2005) 902-904. doi:10.1038/nmeth1205-902.

[2] T. Cordes, S. Blum, Opportunities and challenges in single-molecule and single-particle fluorescence microscopy for mechanistic studies of chemical reactions, Nature Chemistry. 5 (2013) 993-999. doi:10.1038/nchem.1800.

[3] R. Prakash, S. Washburn, R. Superfine, R. Cheney, M. Falvo, Visualization of individual carbon nanotubes with fluorescence microscopy using conventional fluorophores, Applied Physics Letters. 83 (2003) 1219-1221. doi:10.1063/1.1599042.

[4] K. Chen, R. Yan, L. Xiang, K. Xu, Excitation spectral microscopy for highly multiplexed fluorescence imaging and quantitative biosensing, Light: Science &Amp; Applications. 10 (2021). doi:10.1038/s41377-021-00536-3.

[5] C. Foglieni, C. Meoni, A. Davalli, Fluorescent dyes for cell viability: an application on prefixed conditions, Histochemistry And Cell Biology. 115 (2001) 223-229. doi:10.1007/s004180100249.

[6] R. Jain, L. Munn, D. Fukumura, Dissecting tumour pathophysiology using intravital microscopy, Nature Reviews Cancer. 2 (2002) 266-276. doi:10.1038/nrc778.

[7] W. Zhao, S. Tian, L. Huang, K. Liu, L. Dong, J. Guo, A smartphone-based biomedical sensory system, The Analyst. 145 (2020) 2873-2891. doi:10.1039/c9an02294e.

[8] R. Sivakumar, N. Lee, Recent progress in smartphone-based techniques for food safety and the detection of heavy metal ions in environmental water, Chemosphere. 275 (2021) 130096. doi:10.1016/j.chemosphere.2021.130096.

[9] A. Roda, E. Michelini, M. Zangheri, M. Di Fusco, D. Calabria, P. Simoni, Smartphone-based biosensors: A critical review and perspectives, Trac Trends In Analytical Chemistry. 79 (2016) 317-325. doi:10.1016/j.trac.2015.10.019.

[10] S. Kim, P. Akarapipad, B. Nguyen, L. Breshears, K. Sosnowski, J. Baker et al., Direct capture and smartphone quantification of airborne SARS-CoV-2 on a paper microfluidic chip, Biosensors And Bioelectronics. 200 (2022) 113912. doi:10.1016/j.bios.2021.113912.

[11] W. Taron, K. Phooplub, S. Sanchimplee, K. Piyanamvanich, W. Jamnongkan, A. Techasen et al., Smartphone-based fluorescent ELISA with simple fluorescent enhancement strategy for Opisthorchis viverrini (Ov) antigen detection in urine samples, Sensors And Actuators B: Chemical. 348 (2021) 130705. doi:10.1016/j.snb.2021.130705.

[12] W. Zhu, G. Pirovano, P. O'Neal, C. Gong, N. Kulkarni, C. Nguyen et al., Smartphone epifluorescence microscopy for cellular imaging of fresh tissue in low-resource settings, Biomedical Optics Express. 11 (2019) 89. doi:10.1364/boe.11.000089.

[13] S. Chung, L. Breshears, A. Gonzales, C. Jennings, C. Morrison, W. Betancourt et al., Norovirus detection in water samples at the level of single virus copies per microliter using a smartphone-based fluorescence microscope, Nature Protocols. 16 (2021) 1452-1475. doi:10.1038/s41596-020-00460-7.

[14] V. Müller, J. Sousa, H. Ceylan Koydemir, M. Veli, D. Tseng, L. Cerqueira et al., Identification of pathogenic bacteria in complex samples using a smartphone based fluorescence microscope, RSC Advances. 8 (2018) 36493-36502. doi:10.1039/c8ra06473c.

[15] C. Song, Y. Yang, X. Tu, Z. Chen, J. Gong, C. Lin, A Smartphone-Based Fluorescence Microscope With Hydraulically Driven Optofluidic Lens for Quantification of Glucose, IEEE Sensors Journal. 21 (2021) 1229-1235. doi:10.1109/jsen.2020.3019889.

[16] M. Sami, M. Tayyab, P. Parikh, H. Govindaraju, U. Hassan, A modular microscopic smartphone attachment for imaging and quantification of multiple fluorescent probes using machine learning, The Analyst. 146 (2021) 2531-2541. doi:10.1039/d0an02451a.

[17] Smartphone based microfluidic biosensor for leukocyte quantification at the Point-of-Care, in: 2019 IEEE Healthcare Innovations And Point Of Care Technologies, (HI-POCT), IEEE, Bethesda, 2019. https://ieeexplore.ieee.org/abstract/document/8962697 (accessed 8 June 2022).

[18] Particle Quantification from a Smartphone-based Biosensor using Deep Convolutional Neural Network for Clinical Diagnosis, in: 2022 IEEE Healthcare Innovations And Point Of Care Technologies (HI-POCT), IEEE, 2022. https://ieeexplore.ieee.org/abstract/document/9744062 (accessed 8 June 2022).

[19] Q. Wei, H. Qi, W. Luo, D. Tseng, S. Ki, Z. Wan et al., Fluorescent Imaging of Single Nanoparticles and Viruses on a Smart Phone, ACS Nano. 7 (2013) 9147-9155. doi:10.1021/nn4037706.

[20] D. RABHA, A. SARMAH, P. NATH, Design of a 3D printed smartphone microscopic system with enhanced imaging ability for biomedical applications, Journal Of Microscopy. 276 (2019) 13-20. doi:10.1111/jmi.12829.

[21] B. Yeniad, S. Yilmaz, L. Bilgin, Evaluation of the microstructure of cornea by in vivo confocal microscopy in contact lens wearing and non-contact lens wearing keratoconus patients, Contact Lens And Anterior Eye. 33 (2010) 167-170. doi:10.1016/j.clae.2010.04.005.

[22] N. Campeau, C. Johnson, J. Felmlee, J. Rydberg, R. Butts, R. Ehman et al., MR imaging of the abdomen with a phased-array multicoil: prospective clinical evaluation., Radiology. 195 (1995) 769-776. doi:10.1148/radiology.195.3.7754009.

[23] B. Siewert, M. Patel, M. Mueller, J. Gaa, D. Darby, C. Poser et al., Brain lesions in patients with multiple sclerosis: detection with echo-planar imaging., Radiology. 196 (1995) 765-771. doi:10.1148/radiology.196.3.7644641.

[24] S. Wolff, R. Balaban, Assessing contrast on MR images., Radiology. 202 (1997) 25-29. doi:10.1148/radiology.202.1.8988186.

[25] M. Adamis, W. Li, P. Wielopolski, D. Kim, E. Sax, K. Kent et al., Dynamic contrast-enhanced subtraction MR angiography of the lower extremities: initial evaluation with a multisection two-dimensional time-of-flight sequence., Radiology. 196 (1995) 689-695. doi:10.1148/radiology.196.3.7644630.